

The [CII] and FIR properties of $z > 6$ radio-loud quasars

Y. Khusanova[1], E. Bañados[1], C. Mazzucchelli[2], S. Rojas-Ruiz[1⋆], E. Momjian[3], E. P. Farina[4], R. Decarli[5], F. Walter[1], B. Venemans[6], F. Wang[7], and J. Yang[7]

[1] Max-Planck-Institut für Astronomie, Königstuhl 17, D-69117 Heidelberg, Germany
[2] European Southern Observatory, Alonso de Cordova 3107, Vitacura, Region Metropolitana, Chile
[3] National Radio Astronomy Observatory, PO Box O, Socorro, NM 87801, USA
[4] Gemini Observatory, NSF's NOIRLab, 670 N A'ohoku Place, Hilo, Hawai'i 96720, USA
[5] INAF - Osservatorio di Astrofisica e Scienza dello Spazio di Bologna, via Gobetti 93/3, I-40129, Bologna, Italy
[6] Leiden Observatory, Leiden University, PO Box 9513, 2300 RA Leiden, The Netherlands
[7] Steward Observatory, University of Arizona, 933 N. Cherry Ave., Tucson, AZ 85721, USA

March 16, 2022

ABSTRACT

There are only five $z > 6$ radio-loud quasars currently known and their rest-frame far-infrared (FIR) properties have not been explored in detail. We present a NOEMA survey of [CII] (158 μm) and underlying continuum emission of four $z > 6$ radio-loud quasars. They reveal diverse properties. J0309+2717 ($z = 6.10$) has a bright [CII] line and underlying continuum, resulting in an starburst with star-formation rate SFR=340–1200 $M_\odot\,\mathrm{yr}^{-1}$. J1429+5447 ($z = 6.18$) has a SFR=$520 - 870\,M_\odot \mathrm{yr}^{-1}$ and its [CII] profile is consistent with two Gaussians, which could be interpreted as a galaxy merger. J1427+3312 ($z = 6.12$) has a moderate SFR = 30–90 $M_\odot\,\mathrm{yr}^{-1}$. Notably, this is a broad absorption line quasar and we searched for a presence of high-velocity outflows in the host galaxy. Although the NOEMA data reveals a tentative broad component of the [CII] line as wide as ∼1400 km s^{-1}, the sensitivity of current data is not sufficient to confirm it. Finally, P172+18 ($z = 6.82$) is undetected in both [CII] and continuum, implying a SFR$< 22 - 40\,M_\odot \mathrm{yr}^{-1}$. The broad range of SFRs is similar to what is observed in radio-quiet quasars at similar redshifts. However, the radio jets can contribute to both [CII] and IR luminosities and if that contribution is significant, the derived SFRs of galaxies hosting radio-loud quasars can be on average lower than in radio-quiet quasars, indicative of a negative feedback from the radio jet.

1. Introduction

The formation and evolution of supermassive black holes is one of the key unresolved puzzles in astrophysics. Already in the first Gyr of the Universe, black holes (BHs) of masses $\sim 10^9 M_\odot$ are in place (e.g., Bañados et al. 2018b; Yang et al. 2020; Wang et al. 2021). It is still a mystery how these BHs acquire such masses and how their evolution is connected to that of the host galaxies (e.g., Inayoshi et al. 2020; Volonteri et al. 2021). The mergers of host galaxies can lead to a coalescence of the BHs. Mergers are also thought to play a role in driving the gas towards the center, thus enabling efficient accretion onto the BH. This can result in the formation of radio-jets (e.g. Chiaberge et al. 2015). The presence of a radio-jet allows to partially convert accretion power to non-radiative form thus enhancing the accretion rate (e.g., Jolley & Kuncic 2008). Hence, mergers of host galaxies and possible subsequent formation of radio-jets can play a crucial role in the fast growth of BHs in the early Universe (Volonteri et al. 2015).

Quasars are traditionally divided into radio-quiet and radio-loud. One of the most common definition of radio-loudness is $R_{4400} = S_{5GHz}/S_{4400\text{Å}}$, where S_{5GHz} and S_{4400} are flux densities at the rest-frame at 5 GHz and 4400 Å, respectively (Kellermann et al. 1989). The quasars with $R_{4400} > 10$ are considered radio-loud and is a sign of the existence of powerful jets. The host galaxies of radio-quiet quasars at $z \gtrsim 6$ have been extensively observed using the Atacama Large Millimeter/submillimeter Array (ALMA) and the NOrthern Extended Millimeter Array (NOEMA) revealing the cold dust emission in the rest-frame far-infrared (FIR) and [CII] line emission (e.g. Wang et al. 2013; Willott et al. 2015; Bañados et al. 2015a; Willott et al. 2017; Decarli et al. 2018; Izumi et al. 2018, 2019; Venemans et al. 2020). These studies showed that the host galaxies of radio-quiet quasars have star formation rates (SFRs) reaching up to 2500 M$_\odot$/yr (e.g., Decarli et al. 2018) and one third shows signs of recent mergers (Neeleman et al. 2021). Many studies have been made to find active galactic nuclei (AGN) driven outflows in the host galaxies but the results are still inconclusive (Cicone et al. 2015; Bischetti et al. 2019; Novak et al. 2020; Meyer et al. 2022). All these questions, whether the host galaxies have outflows, how common are mergers among host galaxies and how the AGN feedback affects star formation were unaddressed for the population of radio-loud quasars at $z > 6$. Therefore, it is still unknown whether the host galaxies of radio-loud quasars differ from those of radio-quiet ones.

The presence of radio-jets can affect the evolution of the host galaxies in different ways. While AGN-driven extreme gas outflows can lead to quenching of star formation in the host galaxy (e.g., Di Matteo et al. 2005; Villar Martín et al. 2014), these jets can also trigger enhanced star formation in the host galaxy via AGN-induced pressure (e.g., Silk 2013). It is unclear which mechanism plays the most

⋆ Fellow of the International Max Planck Research School for Astronomy and Cosmic Physics at the University of Heidelberg (IMPRS-HD).

important role at high redshift, since no systematic study of host galaxies of radio-loud quasars at $z \gtrsim 6$ has been done. Compared to radio-quiet quasars, they are rare, they constitute only 8-10% of quasar population at $z \gtrsim 6$ (Bañados et al. 2015b; Liu et al. 2021). To date there are only five radio-loud quasars known at $z > 6$: J1427+3312 at $z = 6.12$ (McGreer et al. 2006), J1429+5447 at $z = 6.18$ (Willott et al. 2010), J0309+2717 at $z = 6.10$ (Belladitta et al. 2020), J2318–3113 at $z = 6.44$ (Ighina et al. 2021) and P172+18 at $z = 6.83$ (Bañados et al. 2021). Only the rest-frame FIR properties of one of them, J2318–3113, have been studied but before this source was recognized as radio-loud (Decarli et al. 2018; Venemans et al. 2020; Neeleman et al. 2021).

In this paper, we report NOEMA observations of [CII] emission and the underlying continuum for the remaining 4 radio-loud quasars known at $z > 6$. In Section 2, we describe the observations and data reduction. In Section 3, we present the results for individual objects and discuss their properties. In Section 4, we compare the [CII] emission and dust properties of all currently known $z \gtrsim 6$ radio-loud quasars with the samples of radio-quiet quasars at $z \gtrsim 6$ from the literature. Finally, in Section 5 we present our conclusions. Throughout the paper we use ΛCDM cosmology with $\Omega_\Lambda = 0.70$, $\Omega_m = 0.30$ and $h = H_0/100 = 0.7$.

2. Data

We have observed four out of five known $z > 6$ radio-loud quasars with NOEMA. J1427+3312, J1429+5447 and P172+18 were observed in 2019, December 3rd, June 16th and August 14th, as part of the S19DN observing programme. J0309+2717 was observed in 2020, June 18th, 20th and July 20th as part of the S20CY observing programme. All targets were observed in band 3, which covers $\sim 208 - 264$ GHz range where the redshifted [CII] emission line falls at $z \gtrsim 6$. The tuning frequencies were chosen so that the [CII] emission falls in one of the side bands. The other side band can be used for FIR continuum emission measurements.

The observations were carried out using configurations C, D or a combination of the two, which allows to maximize the sensitivity for a detection experiment. Most observations were carried out with 10 antennas, except for J1429+5447 and one of the tracks for J1427+3312, for which 9 antennas were used. The beam sizes (0.5–1.7 arcsec) correspond to 3–10 kpc at the quasar redshifts. The total integration time, configuration used, and synthesized beam for each quasar are listed in Table 1.

The data were calibrated using the standard calibration steps in GILDAS software[1]. We used 3C84, 3C345, 3C273 or 3C279 sources for bandpass calibration. The phase and amplitude were calibrated with 1417+273, 1418+546, 1147+245. The flux was calibrated using LKHA101 for P172+18 and MWC349 for the rest of the sample. We flagged bad visibilities before producing the uv tables. We resampled all uv tables to the resolution of 50 km s^{-1}.

The dirty images were produced from the uv tables using *MAPPING* software package (part of GILDAS). We used natural weighting, since we expect that our targets will not be resolved and they are exactly at the center of the image where natural weighting yields the optimal sensitivity. The clean images were produced using the HOGBOM method (Högbom 1974) in *MAPPING*. The resulting data cubes were saved in FITS format for further analysis.

First, we collapsed all channels in the cubes to produce preliminary images. We found $>3\sigma$ detections in the center of the images of J1427+3312, J1429+5447 and J0309+2717. We then extracted spectra from the brightest pixel on the collapsed image to search for [CII] emission line. We found $>3\sigma$ [CII] line detections for all targets where emission was detected on a collapsed image. We produced continuum maps using the side band, which is free from [CII] emission, by averaging all channels in this band. We used the publicly available code Interferopy (Boogaard et al. 2021) to measure flux density using the residual scaling method described in Novak et al. (2020). In this method the flux density measured on the clean map is corrected by scaled residual flux density. The scaling factor is defined as the clean-to-dirty beam area ratio. We extracted the spectra from the brightest pixel. Since no significant emission was found on the collapsed image of P172+18, we extracted spectra from the central pixel that is located at the optical position of the quasar (Banados et al. 2021) . We also extracted spectra using different circular apertures and determined the optimal radius by analysing their curves of growth. We chose the aperture radius, at which increasing the radius changes the measured peak flux density only within the error bars of flux measured inside the aperture. We start with an aperture size equal to the half of the semi-major axis of the beam. This is also the aperture size which we used in case of non-detection. In this way, we make sure that we do not miss any flux of an unresolved source and do not introduce additional noise if we chose a bigger aperture. In the same way, we chose the aperture for measuring continuum flux density. The apertures were centered on the brightest pixel coincident with the center of the image. Initially, we fit all the [CII] emission line profiles detected with a single Gaussian. We estimated continuum emission excluding all channels within ±1000 km s^{-1} from the peak of the [CII] line. We subtracted continuum using the task *UV_BASELINE* in *MAPPING*. We then produced integrated [CII] line maps using channels containing the line across 1.2×FWHM.

3. Results

Our analysis reveals a range of host galaxy properties of radio-loud quasars. The [CII] line and underlying continuum were detected for J1427+3312, J1429+5447, J0309+2717, while they were not detected for P172+18 as discussed in more detail below. The [CII] and underlying continuum emission line measurement results are summarized in Table 2. Fig. 1 shows the 250 GHz continuum and [CII] line maps and the spectra zoomed on the [CII] emission line. Below we discuss results of each individual object in the sample ordered by their redshift.

3.1. J0309+2717 ($z = 6.10$)

J0309+2717 is the most radio-loud quasar at $z > 6$. Based on its radio and X-ray properties, this source was classified as a blazar and currently it is the only blazar at $z > 6$ (Belladitta et al. 2020). It has the brightest 250 GHz continuum emission in our sample ($F_{\rm cont} = 4.39 \pm 0.15$ mJy) and

[1] https://www.iram.fr/IRAMFR/GILDAS

Table 1. NOEMA observations

Quasar	R_{4400} [a]	Integration time (hours)	Configuration	Beam size (arcsec)
J0309+2717	2500 ± 500 [b]	4.8	D	1.7×1.1
J1427+3312	53.3 ± 4.1 [c]	3.4	CD	1.1×0.7
J1429+5447	109.2 ± 4.1 [c]	3.4	D	1.6×1.4
P172+18	70 ± 7 [d]	4.1	C	1.1×0.5

Notes. [(a)] Radio-loudness $R_{4400} = S_{5GHz}/S_{4400\text{Å}}$ (Kellermann et al. 1989). [(b)] Belladitta et al. (2020) [(c)] Bañados et al. (2015b) [(d)] Bañados et al. (2021)

Table 2. [CII] and underlying continuum emission measurements of the sample presented in this paper and from the radio-loud quasars at $z \gtrsim 6$ in the literature

Quasar	$z_{[CII]}$	F_{cont} (mJy)	$F_{[CII]}$ (Jy km s^{-1})	FWHM (km s^{-1})
J0309+2717	6.100 ± 0.002	4.39 ± 0.15	2.6 ± 0.2	240 ± 20
J1427+3312	6.118 ± 0.006	0.18 ± 0.05	0.7 ± 0.1	440 ± 69
J1429+5447	6.190 ± 0.004	3.05 ± 0.11	3.6 ± 0.2	359 ± 24
P172+18	$6.823^{+0.003}_{-0.001}$ [a]	<0.34 [b]	<0.21 [b]	–
J2318-3113 [c]	6.4429 ± 0.0003	0.36 ± 0.08	1.52 ± 0.14	344 ± 34
P352-15 [d]	5.832 ± 0.001	0.34 ± 0.04	1.37 ± 0.22	440 ± 80

Notes. [(a)] This redshift is measured based on MgII emission line (Bañados et al. 2021). [(b)] The limits are at 3σ and assuming FWHM=350 km s^{-1}. [(c)] The measurements are taken from Venemans et al. (2020) [(d)] The measurements are taken from Rojas-Ruiz et al. (2021)

the second brightest [CII] line emission ($F_{\text{[CII]}} = 2.6 \pm 0.2$ Jy km s^{-1}). The source is unresolved. No significance difference in shape is observed between the spectrum extracted from the brightest pixel and from an aperture with 3.4″ diameter (see Fig. 1). But the spectra extracted with an aperture has higher flux density, since some of the flux is missed if a single pixel is used to extract the spectrum. Therefore, we use the aperture extracted spectrum in further analysis in Section 4.

3.2. J1427+3312 ($z = 6.12$)

J1427+3312 is the first radio-loud quasar discovered at $z > 6$ (McGreer et al. 2006). After the discovery, two independent Very Long Baseline Interferometry (VLBI) follow-up studies of J1427+3312 were conducted. Momjian et al. (2008) observed a structure with two continuum components at 1.4 GHz, separated by 176 pc. Frey et al. (2008) observed J1427+3312 at 1.6 and 5 GHz and the 1.6 GHz observations revealed a double structure of this quasar with two components separated by 160 pc, comparable to the separation observed by Momjian et al. (2008). Both these studies conclude that these two components could be the radio lobes and J1427+3312 could be a Compact Symmetric Object (CSO, Conway 2002). Based on its rest-frame ultraviolet (UV) spectrum, this source was also classified as Broad Absorption Line (BAL) quasar (McGreer et al. 2006; Shen et al. 2019).

Our NOEMA observations reveal only faint [CII] line emission with $F_{[CII],int} = 0.7 \pm 0.1$ Jy km s^{-1}. The curve of growth analysis shows that even with the small aperture the noise in the spectrum significantly increases compared to the extraction from a single pixel. In Fig. 1, we show both the spectrum extracted from the brightest pixel and from the aperture equal to the beam size. The line is visible on both spectra but the peak flux is significantly lower on the spectrum extracted with an aperture due to the noise. On the integrated image (including only the channels containing the line across 1.2×FWHM), the [CII] emission is detected with a 4σ significance. In the channel corresponding to the peak of the line, the significance of the line is 8σ. The emission is unresolved at the resolution of our observations. The 250 GHz continuum has a flux density $F_{cont} = 0.18 \pm 0.05$ mJy.

3.3. J1429+5447 ($z = 6.19$)

J1429+5447 is one of the most studied objects in our sample. Radio observations of J1429+5447 cover the range from 120 MHz (Shimwell et al. 2019) to 1.6 GHz (Frey et al. 2011). The high resolution VLBI observations of this quasar show a compact structure with a size <100 pc. It was also observed at 32 GHz (Wang et al. 2011). These observations targeted CO (2–1) emission line and they tentatively suggest a presence of a companion galaxy separated by 6.9 kpc. Recently, J1429+5447 was also observed with eROSITA and currently it is the brightest X-ray source at $z > 6$.

J1429+5447 is the second brightest quasar in our sample at ∼250 GHz ($F_{cont} = 3.05 \pm 0.11$ mJy) and has the brightest [CII] emission line ($F_{[CII],int} = 3.6 \pm 0.2$ Jy km s^{-1}). Interestingly, when we extract the spectrum with an aperture, thus accounting for all the flux seen on the [CII] line image, additional flux, deviant from the fit with a single Gaussian appears. This can be an evidence of existence of a companion galaxy with a broader [CII] line emission or an outflow. We will discuss this in more detail in Section 4.1.

3.4. P172+18 ($z = 6.82$)

P172+18 is the highest redshift quasar in our sample and the highest redshift radio-loud quasar known to date. It

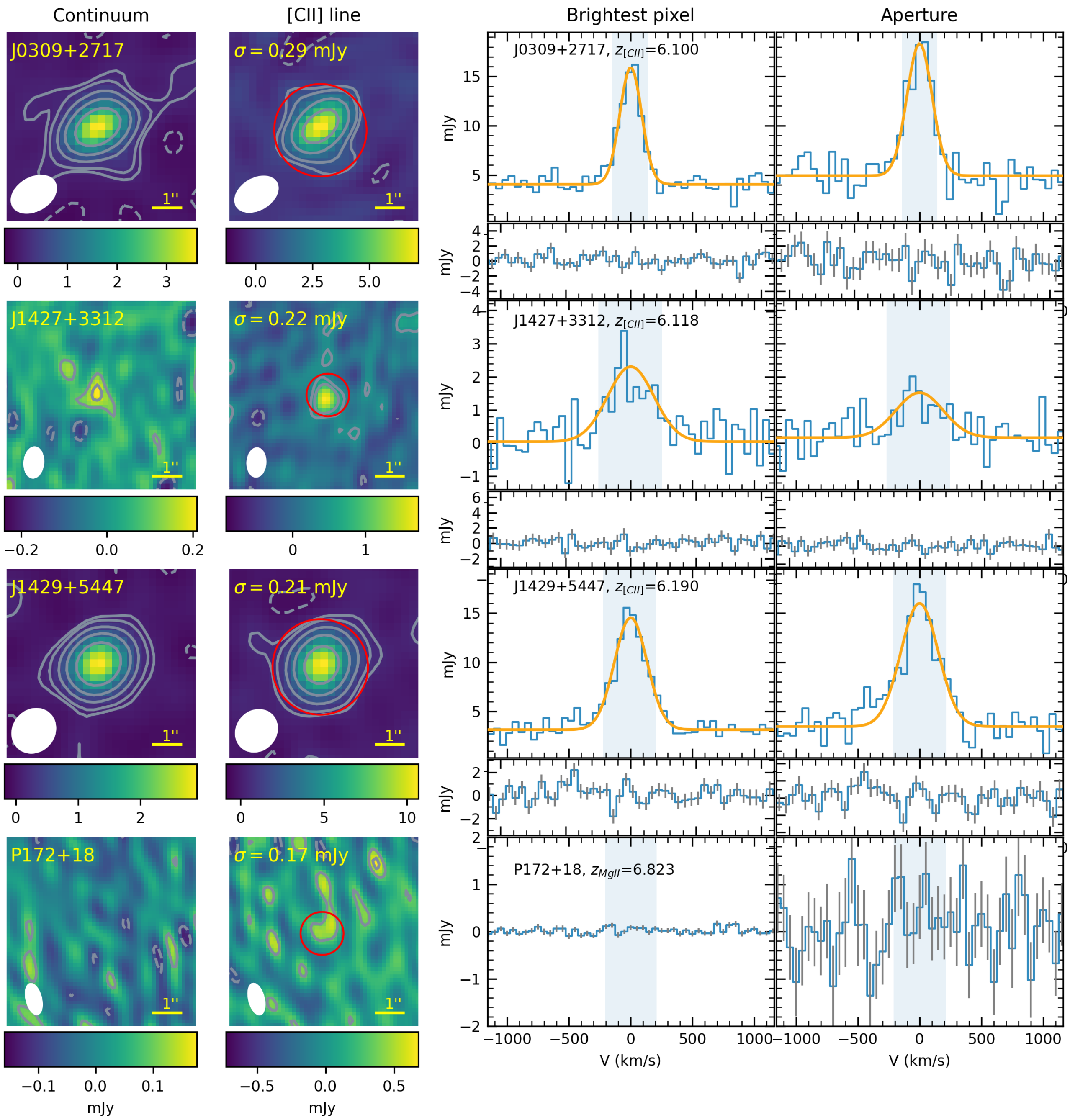

Fig. 1. The images and spectra of the radio-loud quasars in our sample. First column: the 250 GHz continuum images. The contour levels are (-2, 2, 3.5, 8, 16, 32)$\times\sigma$ where σ = 0.05 mJy. Second column: The integrated [CII] line images (continuum subtracted). The countour levels are (-2, 2, 3.5, 8, 16, 32)$\times\sigma$ and σ values are shown on images. The contour levels are the same as in the first column. The red circles show the apertures, from which the spectrum in the fourth column was extracted. Third column: Spectra from the brightest (central) pixel. The solid orange line shows the best fit to the line with a Gaussian. The shaded area shows the channels used to create the integrated maps on the second column. Fourth column: spectra extracted using the apertures shown in images in the second column (see Section 2).

is the only source from our sample, which is not detected in both [CII] and continuum emission (see Fig. 1). The 3σ upper limit for the FIR continuum flux density is $F_{cont} < 0.34$ mJy. We determine the upper limit for [CII] emission assuming the mean FWHM of [CII] emission line in the host galaxies of radio-quiet quasars at $z > 6$ FWHM=350 km s^{-1} (Decarli et al. 2018; Venemans et al. 2020). The 3σ upper limit with this assumption is $F_{[CII],int} < 0.21$ Jy km s^{-1}.

Table 3. The statistical criteria values for selection between the fit with one Gaussian and two Gaussians.

Quasar	$\Delta\chi^2$	p-value	ΔAIC[a]	ΔBIC[a]
J0309+2717	4.99	0.82738	0.47	-10.83
J1427+3312[b]	0.92	0.17997	-3.82	-10.93
J1427+3312[c]	1.33	0.27680	-1.1	-8.21
J1429+5447	23.08	0.99996	10.02	2.91

Notes. [(a)] Negative values imply preference for the fit with one Gaussian; positive values imply preference for the fit with two Gaussians. [(b)] The spectrum extracted from the brightest pixel [(c)] The spectrum extracted with an aperture

4. Discussion

4.1. Are host galaxies of radio-loud quasars mergers or outflows?

At redshifts $1 < z < 2.5$, 92% of radio-loud quasars are hosted in merging galaxies compared to 38% of radio-quiet quasars (Chiaberge et al. 2015). The merger fraction of radio-quiet quasars at $z \gtrsim 6$ is 31% (Neeleman et al. 2021). This suggests no evolution with redshift of the merger fraction. In that case, most host galaxies of radio-loud quasars at $z \gtrsim 6$ should be mergers. The recently identified $z = 6.44$ radio-loud quasar J2318–3113 (Ighina et al. 2021) was already observed by ALMA with high resolution and its kinematics and morphology were studied in detail by Neeleman et al. (2021). They find that J2318–3113 has a disturbed morphology indicative of a recent or ongoing merger activity (see Fig. 2 in Neeleman et al. 2021).

We noted in Section 3 that the [CII] spectrum of J1429+5447 has a broader component, when extracted with an aperture. We fit this spectrum with two Gaussians. The two components have redshifts $z_{broad} = 6.19 \pm 0.009$ and $z_{narrow} = 6.19 \pm 0.003$ and FWHM$_{broad} = 650 \pm 128$ km s^{-1} and FWHM$_{narrow} = 253 \pm 38$ km s^{-1}. The fit with two components is preferred by both Akaike Information Criterion (AIC) and Bayesian Information Criterion (BIC, the values are listed in Table 3), although the BIC difference does not exceed the threshold ΔBIC > 10 for a strong significance (Kass & Raftery 1995). The χ^2 difference implies p-value of $p = 0.99996$ for three additional degrees of freedom or 3.95σ significance for a broad component.

Previously, CO (2–1) emission line of J1429+5447 was observed with resolution ~0.7 arcsec at 32 GHz with Expanded Very Large Array (EVLA). Wang et al. (2011) report a presence of two components of CO (2–1) emission line where the broad component is detected at 4σ significance. The two components have redshifts $z_{east} = 6.1837$ and FWHM$_{east} = 400$ km s^{-1}, and $z_{west} = 6.1831$ and FWHM$_{west} = 280$ km s^{-1}. The widths and redshifts of the CO (2–1) line are consistent with the ones we obtained from the best fit of the [CII] line profile on the spectrum from the aperture. The similarity of the widths of the spectral profiles of the CO(2–1) and [CII] lines suggests that the [CII] emission arises from the same structure as the reported CO (2–1) emission. In that case, J1429+5447 is likely to be a merger or two gravitationally interacting sources.

We cannot completely separate the narrow component from the broad one, but by averaging the channels within 1.2×FWHM of the broad component and excluding all the channels across 1.2×FWHM of a narrow component, we can obtain an image with little contamination from a narrow component. In order to obtain an image of the narrow component, we average the channels across 1.2×FWHM$_{narrow}$. These channels still contain emission from the broad component, but the emission from the narrow component is comparable to the broad one or dominates it. We show the images for the narrow and broad components in Fig. 2. The images of broad and narrow component still overlap and we cannot make firm conclusions, whether they could be separated as the CO(2–1) line emission observed by Wang et al. (2011). The size of the NOEMA beam is 1.6×1.4 arcsec, almost two times larger than the beam of the CO(2–1) line observations and larger than the separation between the components on the CO(2–1) line map. Since the broad component of J1429+5447 is more prominent on the spectra extracted with a larger aperture (if we place the aperture on the center of the image), this emission can also arise from a [CII] halo and not from a second separate component. Therefore, higher resolution [CII] observations are necessary to make firm conclusions about the nature of the broad and narrow [CII] emission in this system.

The existence of the outflows in host galaxies of radio-quiet quasars is debated in the literature. Individual radio-quiet quasars observed at $\nu_{rest} \sim 1900$ GHz predominantly have single Gaussian profiles of [CII] line with FWHM$_{[CII]} \sim 350$ km s^{-1} (Decarli et al. 2018; Novak et al. 2020). Maiolino et al. (2012) and Cicone et al. (2015) found such outflows in a host galaxy of J1148+5251, but later observations of this object by Meyer et al. (2022) with a larger number of antennas and new wide-band correlator PolyFiX of NOEMA did not confirm the presence of outflows in the host galaxy. (Bischetti et al. 2019) approached the search of outflows using the stacking of ALMA cubes. The stacked spectrum revealed evidence of a weak broad component with FWHM$^{broad}_{[CII]} = 1730 \pm 210$ km s^{-1} (Bischetti et al. 2019). However, this is a delicate issue that might depend on different techniques employed. The stacking analysis by Bischetti et al. (2019) was done in the image plane, while Novak et al. (2020) used the stacking in the uv-plane and did not find any evidence for a presence of the broad component. While the spectral profile of J1429+5447 has indication of a narrow and a broad component, the width of the broad component is much smaller than what is typical for the outflows (i.e., a few 1000s km s^{-1}).

We performed a similar analysis for the remaining quasars with a [CII] detection in our sample. J0309+2717 has no indication of a second component. The fit with two Gaussians is discarded by BIC and the difference in AIC is not significant (see Table 3). The χ^2 difference corresponds to 0.94σ significance of the broad component. Since the fit with two Gaussians does not have a physical meaning in case of J0309+2717, we conclude that its spectrum is represented by one Gaussian.

J1427+3312 was previously classified as BAL quasar (McGreer et al. 2006; Shen et al. 2019). Hence, the host

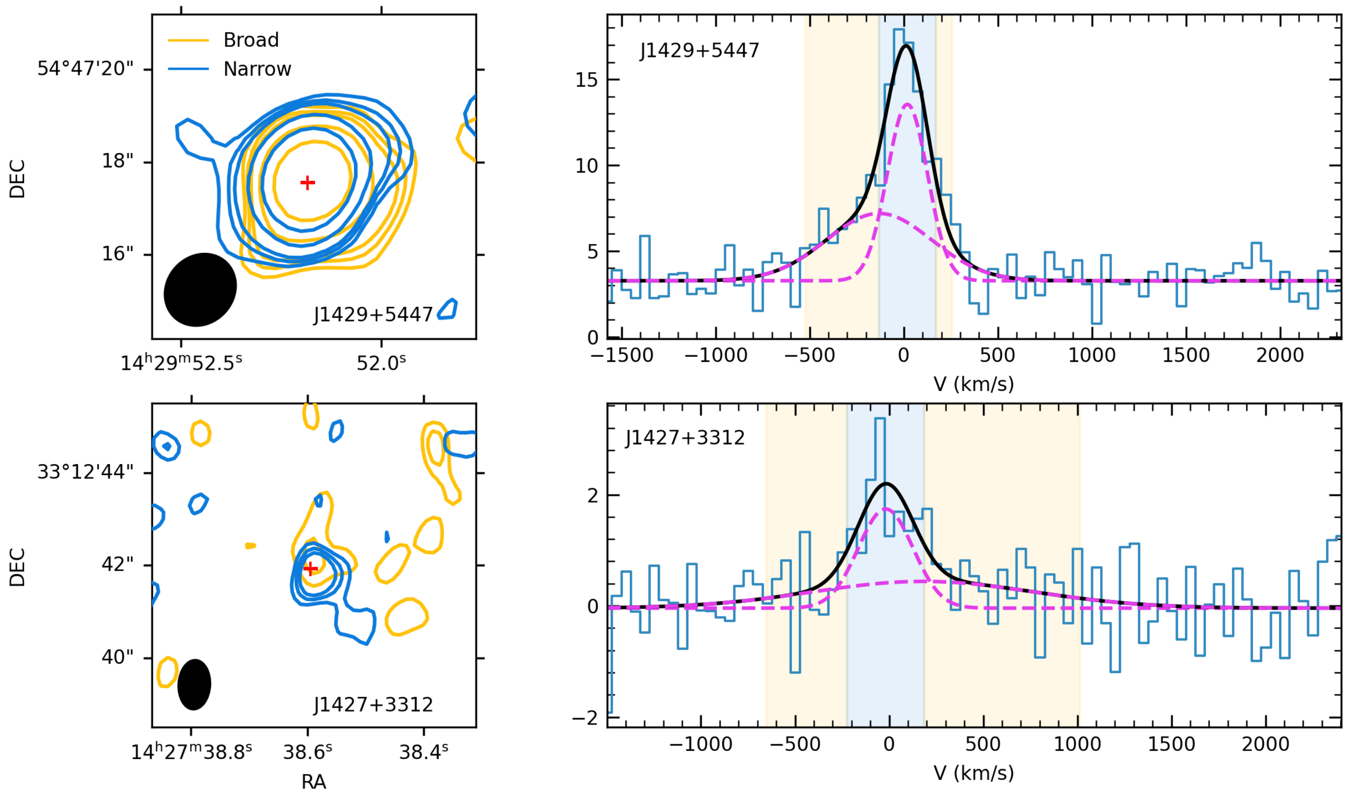

Fig. 2. The images of the broad and narrow components and the spectra of J1429+5447 (*top*) and J1427+3312 (*bottom*). First column: the contours on the images (blue for the narrow and yellow for the broad component). The contours correspond to (2,3,4,8,16)$\times\sigma$. Second column: the spectra (blue line) and the fit with two Gaussians (black solid line). The magenta dashed lines are broad and narrow components of the fit with two Gaussians. The shaded areas shows the channels used to produce corresponding images of the broad and narrow components.

galaxy of this quasar can have high-velocity outflows. In Section 3, we noted that extracting the spectrum with an aperture results in a lower signal to noise ratio (SNR). Therefore, we test the fit with one and two Gaussians on both the spectrum extracted from the brightest pixel and from the aperture. The fit with two Gaussians on the spectrum extracted from the brightest pixel reveals a broad component of [CII] emission with FWHM$_{broad}$ $\sim$ 1400 km s^{-1}. The narrow component has FWHM$_{narrow}$ $= 343 \pm 113$ km s^{-1} consistent with the width of the fit with a single Gaussian. The width of the broad component is consistent with what is expected for outflows. We separate them in the same way as described above and show in Fig. 2. The broad component only has a 3σ emission close to the optical position of the quasar. The fit with two Gaussians, however, is discarded by statistical criteria we used (see Table 3).

We analyse the spectrum extracted with the aperture in the same way. The broad and narrow component of the fit to this spectrum have widths FWHM$_{broad}$ $= 940 \pm 385$ km s^{-1} and FWHM$_{narrow}$ $= 101 \pm 49$ km s^{-1}. The width of the broad component is again consistent with expectations for the outflows. We produce the image of the broad component including the channels in range 1.2$\times$FWHM$_{broad}$. Since the narrow component of this fit is significantly narrower than the previous one, we exclude the same range of channels as above to avoid adding additional flux to the broad component. This image also contains 3σ emission close to the optical position of the quasar. The statistical criteria discard the fit with two Gaussians. However, in case of the spectrum extracted with an aperture, the BIC and AIC difference do not reach the threshold value -10 for strong preference for a single Gaussian. Since the [CII] emission line of J1427+3312 is rather faint and the SNR is low with the sensitivity of our observations, the presence of high-velocity outflows in J1427+3312 requires further investigation with the follow-up observations with higher sensitivity.

4.2. The effects of the jet on star formation

The presence of radio-jets can enhance as well as quench SFR in the host galaxy. Mandal et al. (2021) suggest that both effects are present with increased SFR closer to the center of the host galaxy and decreased on the outskirts. The IR and [CII] observations have been extensively used to estimate SFRs of host galaxies of radio-quiet quasars. Their SFRs reach up to $\sim$2500 M$_\odot$/yr with a median of SFR distribution at $\sim$250 M$_\odot$/yr (e.g. Decarli et al. 2018; Venemans et al. 2020). Here we compare these results with our measurements for the host galaxies of $z \gtrsim 6$ radio-loud quasars.

To determine the IR luminosities, we use the modified black body model (MBB) and optically thin approximation (Beelen et al. 2006):

$$S_{\nu_{obs}} = f_{CMB}\frac{1+z}{D_L^2}\kappa_d(\nu_{rest},\beta)\frac{2h\nu_{rest}^3}{c^2}\frac{M_{dust}}{e^{h\nu_{rest}/k_b T_{dust,z}}-1},$$

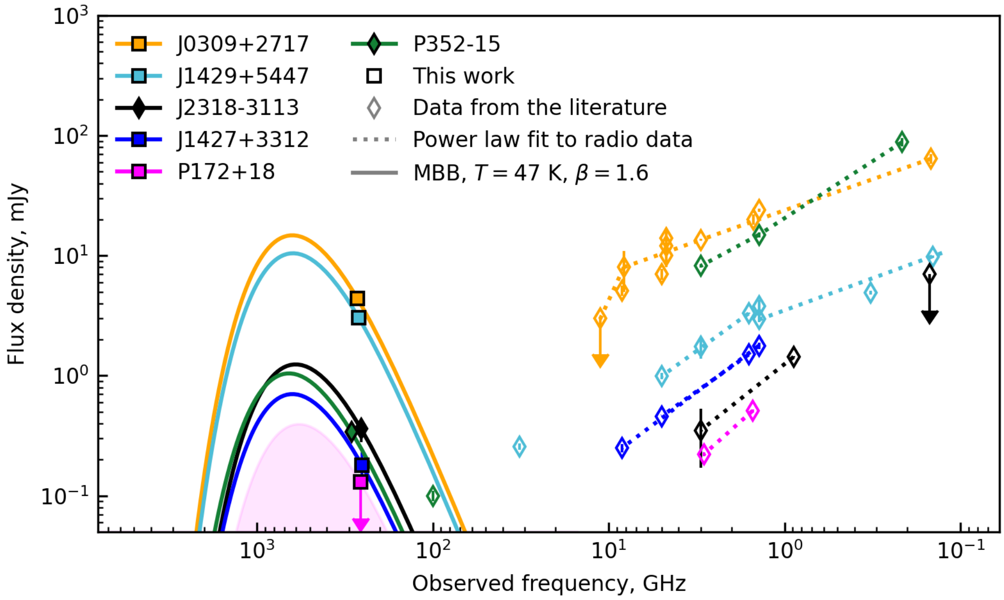

Fig. 3. SEDs of all known radio-loud quasars at $z > 6$ and P352–15 at $z = 5.832$. The filled symbols are measurements of the 250 GHz continuum flux density (NOEMA measurements presented in this paper and literature data from ALMA for J2318-3113 Decarli et al. 2018). The solid lines are MBB model (with $T_{dust} = 47$ and $\beta = 1.6$) scaled to the observed continuum flux density. The dotted lines are the power law (broken power law in the case of J0309+2717 and J1429+5447) fits to the radio data from the literature (Bañados et al. 2021; Condon et al. 1998; Frey et al. 2008, 2011; Ighina et al. 2021; Intema et al. 2017; Momjian et al. 2008; Shimwell et al. 2019; Wang et al. 2011). The literature data are shown with thin diamonds and the NOEMA data for our sample with squares. Different colors correspond to each of the radio-loud quasars as indicated in the legend. The shaded area shows the region below the 3σ limit for continuum flux density of P172+18, which is not detected with NOEMA.

(1)

where f_{CMB} is a correction for the Cosmic Microwave Background (CMB) contrast, D_L is the luminosity distance, $\kappa_d(\nu_{rest}, \beta) = \kappa_{d(\nu_0)}(\nu_{rest}/\nu_o)^\beta$ cm^{2}g^{-1} is the opacity law, M_{dust} is the dust mass, $T_{dust,z}$ is the dust temperature at given redshift, β is the emissivity index and $\nu_{rest} = (1+z)\nu_{obs}$ is the rest frame frequency. For the opacity law, we assume values $\kappa_{d(\nu_0)} = 2.64$ m^{2}kg^{-1} at $\nu_0 = c/(125\mu m)$ from Dunne et al. (2003). The dust temperature heated by the CMB is:

$$T_{dust,z} = (T_{dust}^{\beta+4} + T_{CMB,z=0}^{\beta+4}[(1+z)^{\beta+4} - 1])^{\dfrac{1}{\beta+4}}, \quad (2)$$

where T_{dust} is the intrinsic dust temperature and $T_{CMB,z=0}$ is the CMB temperature at $z = 0$ (da Cunha et al. 2013). Here, we assume $T_{dust} = 47$ K and the emissivity index $\beta = 1.6$ (Beelen et al. 2006). The CMB contrast is defined as:

$$f_{CMB} = 1 - \frac{B_{\nu_{rest}}(T_{CMB,z})}{B_{\nu_{rest}}(T_{dust,z})} \quad (3)$$

where $T_{CMB,z}$ is the CMB temperature at redshift z and $B_{\nu_{rest}}$ is the black body radiation spectrum. We scale the MBB to the continuum flux density at $\nu_{rest} \sim 1900$ GHz and obtain the IR luminosity by integrating between 8 μm and 1000 μm (see Fig. 3). We convert the IR luminosity to SFR using the Kennicutt (1998) relation:

$$SFR_{IR} = \kappa_{IR} L_{IR}, \quad (4)$$

where L_{IR} is the IR luminosity and $\kappa_{IR} = 10^{-10} M_\odot \mathrm{yr}^{-1} L_\odot^{-1}$ is a conversion factor assuming Chabrier (2003) initial mass function.

We use De Looze et al. (2014) relation to convert [CII] luminosities to SFRs:

$$\frac{SFR_{[CII]}}{M_\odot yr^{-1}} = 3 \times 10^{-9} \left(\frac{L_{[CII]}}{L_\odot}\right)^{1.18}. \quad (5)$$

The [CII] luminosities are calculated as

$$\frac{L_{[CII]}}{L_\odot} = 1.04 \times 10^{-3} \frac{F_{[CII]}}{\mathrm{Jy\ km\ s^{-1}}} \frac{\nu_{obs}}{\mathrm{GHz}} \left(\frac{D_L}{\mathrm{Mpc}}\right)^2. \quad (6)$$

where $F_{[CII]}$ are the [CII] line fluxes, ν_{obs} is the observed frequency of the [CII] line and D_L is the luminosity distance (e.g., Carilli & Walter 2013).

Following this approach, we calculated [CII] and IR luminosities of all radio-loud quasars at $z > 6$ and P352–15 at $z = 5.832$(Rojas-Ruiz et al. 2021). We use the data from the literature for J2318–3113 and P352–15, which were previously observed with ALMA(Venemans et al. 2020; Rojas-Ruiz et al. 2021). The results are summarized in Table 4. In Fig. 4, we also show the SFRs of radio-quiet quasars, for which we used as input the observed flux densities reported in the literature (Andika et al. 2020; Bañados et al. 2015a; Decarli et al. 2017, 2018; Eilers et al. 2020; Izumi et al. 2018, 2019; Maiolino et al. 2005; Venemans et al. 2012, 2016, 2017, 2020; Walter et al. 2009; Wang et al. 2013, 2016, 2021; Willott et al. 2013, 2015, 2017; Yang et al. 2019, 2020). We then followed a consistent approach to derive their luminosities and SFRs as described above.

Table 4. The IR and [CII] luminosities and SFRs of radio-loud quasars at $z \gtrsim 6$

Quasar	$\log(L_{IR}/L_\odot)$	$\log(L_{[CII]}/L_\odot)$	$\log SFR_{IR}(M_\odot yr^{-1})$	$\log SFR_{[CII]}(M_\odot yr^{-1})$
J0309+2717	13.07 ± 0.01	9.40 ± 0.03	3.07 ± 0.01	2.57 ± 0.04
J1427+3312	$11.68^{+0.11}_{-0.16}$	$8.82^{+0.06}_{-0.07}$	$1.68^{+0.11}_{-0.15}$	$1.88^{+0.07}_{-0.09}$
J1429+5447	12.92 ± 0.02	$9.55^{+0.02}_{-0.03}$	2.92 ± 0.02	2.75 ± 0.03
P172+18	$< 11.61^a$	$< 8.37^a$	$< 1.61^a$	$< 1.35^a$
J2318–3113[b]	$12.02^{+0.09}_{-0.11}$	9.20 ± 0.04	$2.02^{+0.09}_{-0.11}$	2.33 ± 0.05
P352–15	11.93 ± 0.5	$9.09^{+0.06}_{-0.08}$	1.93 ± 0.5	$2.21^{+0.08}_{-0.08}$

Notes. [(a)] The upper limits are at 3σ [(b)] The flux measurements are taken from Venemans et al. (2020). The luminosities and SFRs are recalculated following the approach in Section 4.2

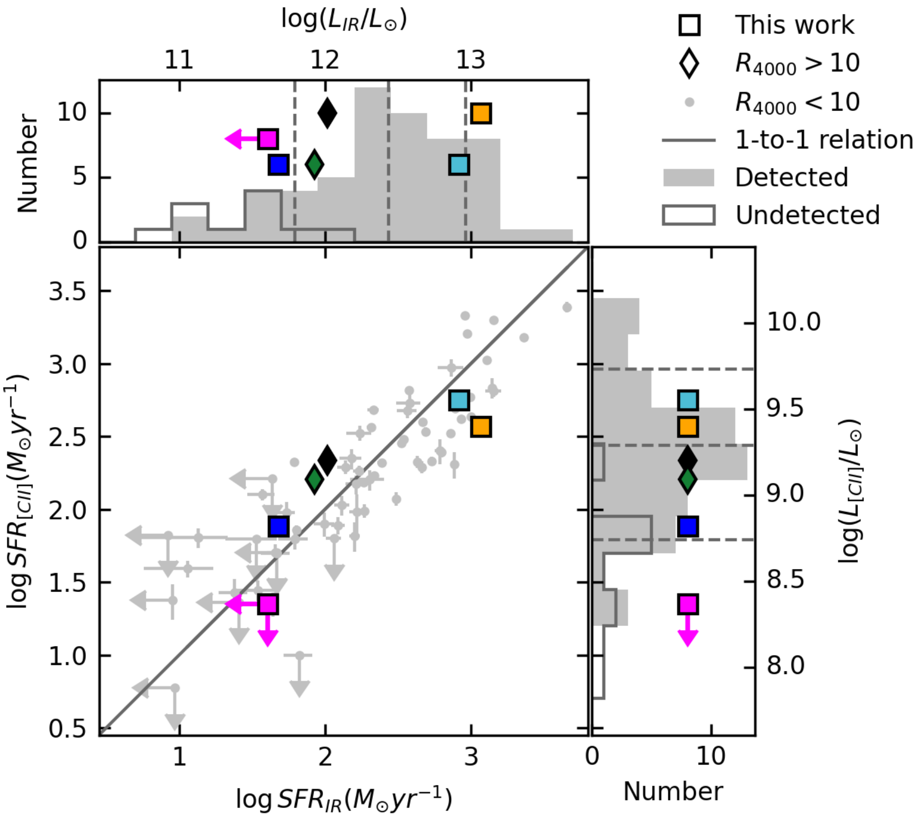

Fig. 4. The SFRs of radio-quiet (grey circles) and radio-loud (colored symbols) quasars at $z \gtrsim 6$ using [CII] and IR luminosities as SFR tracers. The radio-loud quasars from our sample are shown as squares and from the literature as thin diamonds. Colors for radio-loud quasars are the same as in Fig. 3. The solid line shows 1-to-1 relation. The SFR (luminosity) distributions of radio-quiet quasars are shown (grey histograms). The dashed lines show the 16th, 50th and 84th percentiles of the distributions for radio-quiet quasars. References for the literature measurements are in the main text, Section 4.2.

The SFR_{IR} agrees well with the $SFR_{[CII]}$ with a scatter of ~ 0.3 dex around the 1-to-1 relation for both radio-quiet and radio-loud quasars. The [CII] luminosities and $SFR_{[CII]}$ of the radio-loud quasars are in good agreement with the distribution for radio-quiet quasars. This is, however, not the case for IR luminosities and SFR_{IR}. The faintest radio-loud quasars fall all below the 21st percentile of the distribution of radio-quiet quasars, while the brightest are above ~81st percentile. No radio-loud quasar falls within 0.65σ from the median of the SFR_{IR} distribution of radio-quiet quasars. This could be an indication of a bimodal distribution of IR luminosities of radio-loud quasars or simply a result of a small number statistics.

We use two sample Kolmogorov-Smirnov (KS) test to determine, whether the SFRs or radio-quiet and radio-loud quasars come from the same distribution. For $SFR_{[CII]}$, the KS statistic is 0.22 and p-value is 0.94. For SFR_{IR}, the KS statistic is 0.39 and p-value ist 0.4. In both cases, the null hypothesis that the two samples are drawn from the same distribution cannot be rejected. If that is the case, SFR distribution of the radio-loud quasar hosts does not differ significantly from the radio-quiet population. This could mean that the presence of the jet does not have an effect on the SFR or both negative and positive feedback play a role and result in comparable SFRs in the host galaxies of radio-loud quasars.

The role of negative and positive feedback can change depending on the evolutionary stage of the jet. Simulations show that initially the turbulence induced by the jet into the interstellar medium (ISM) causes decrease of the SFR.

Once the jet decouples from the disk, this effect weakens and the positive feedback becomes stronger (Mandal et al. 2021). The ages of the jet were previously estimated for two quasars in our sample. Momjian et al. (2008) estimated the age of J1427+3312 to be $\sim 10^3$ yr based on the typical advance speed of CSOs and the distance between the radio lobes. P172+18 was classified as Compact Steep Spectrum (CSS) radio source (Momjian et al. 2021). Assuming typical advance speed for such objects, the age of the jet of P172+18 is $\sim$ 1700 yr. Both of these quasars with very young jets have faint [CII] and FIR continuum emission and low SFRs, consistent with the expectation that negative feedback plays more important role for younger sources. However, it is necessary to obtain the estimates of the jet age for the remaining quasars in the sample to confirm this scenario.

We note that in deriving SFRs, we assumed that [CII] and IR luminosities are only related to the star formation in the host galaxies. This is a reasonable assumption for radio-quiet quasars at $z \gtrsim 6$ (Venemans et al. 2017; Pensabene et al. 2021), but has not yet been tested for radio-loud ones. If AGN-related sources of [CII] and IR emission are significant, we are overestimating the SFRs.

In our measurements of SFR_{IR}, we assumed that the FIR continuum emission is attributed to the cold dust only. However, this is not always the case for radio-loud quasars. Rojas-Ruiz et al. (2021) shows that the FIR continuum emission of P352–15, one of the most powerful radio-loud quasars known in the early Universe (Bañados et al. 2018a), cannot be reproduced by using a MBB model only. Therefore, the synchrotron emission from the jet can contribute to the FIR continuum emission.

The [CII] emission can arise from photon-dominated region (PDR) associated with the star formation in the host galaxy or from the X-ray dominated region (XDR) where the gas is affected by the X-ray photons from the AGN or from shocks. The X-ray radiation heats the gas and can potentially cause negative AGN feedback on star formation. One way to determine whether XDR contributes to a significant fraction of the [CII] emission is by measuring [CII]/[CI] luminosity ratio. XDR and PDR models show that CI is more abundant in the XDR (e.g. Meijerink et al. 2007). The observations of [CI] and [CII] emission lines in radio-quiet quasars point to the PDR origin of their [CII] emission (e.g., Venemans et al. 2017), but [CI] emission line has not yet been observed for any of the quasars in our sample.

Notably, the two quasars with the brightest [CII] emission in our sample are also the brightest X-ray sources known at $z \gtrsim 6$ (Medvedev et al. 2020, 2021). Their intrinsic X-ray radiation could be lower because X-ray luminosity can be enhanced by the inverse Compton scattering of the CMB photons by electrons in the jets, which is particularly important at high redshift (e.g., Ighina et al. 2021; Connor et al. 2021). Nevertheless, the observed high X-ray luminosities of these two quasars can be an indication of higher XDR contribution to the [CII] emission than in quasars with moderate or low X-ray luminosities.

In addition, [CII] can also arise from shocks produced by interactions between jets and the gas in the host galaxy (e.g., Appleton et al. 2018; Smirnova-Pinchukova et al. 2019) or in mergers, where the shocks occur due to collision of gas rich galaxies (e.g., Appleton et al. 2013; Peterson et al. 2018). All the quasars in our sample have evidence of jets. Therefore it is plausible that a fraction of the [CII] emission observed originates from shocks. In addition, J2318+3113 has been classified as a galaxy merger (Neeleman et al. 2021) and we have proposed J1429+5447 as another candidate where strong gravitational interactions might be happening (see discussion in Section 4.1). The combination of all these effects could explain the bright [CII] emission observed in these two sources.

Our current data do not allow to determine the origin of FIR emission and [CII] line emission and it is possible that both $\mathrm{SFR}_{\mathrm{IR}}$ and $\mathrm{SFR}_{[\mathrm{CII}]}$ are overestimated. If this is the case, the SFRs for radio-loud quasars would then all be below 64th percentile of the distribution for radio-quiet quasars (based on [CII]). The lack of highly star-forming host galaxies can be either due to stronger negative feedback from the jet or just a small number statistics.

5. Conclusions

We presented [CII] and underlying continuum observations of four (out of five known) radio-loud quasars at $z > 6$ with NOEMA. Four radio-loud quasars are robustly detected in [CII] and their underlying continuum (three from our NOEMA survey and one from previous ALMA observations), while P172+18, the highest-redshift radio-loud quasar known to date ($z = 6.8$), remained undetected.

The spectral profiles of [CII] line differ between all three detected host galaxies in our sample. The spectral profile of J1427+3312 is best described by one Gaussian. However, the fit with two Gaussians suggests a possible presence of the broad component with FWHM$\sim 900 - 1400$, which can be associated with high-velocity outflows. The SNR of current data is insufficient to make firm conclusions. J0309+2717 has a spectral profile represented by a single Gaussian, similar to what is observed in radio-quiet quasars. J1429+5447 has clear signature of two components with widths $\mathrm{FWHM}_{broad} = 650 \pm 128$ km s^{-1} and $\mathrm{FWHM}_{narrow} = 253 \pm 38$ km s^{-1}. Based on their similarity to CO (2–1) line observed with EVLA (Wang et al. 2011), we conclude that the host galaxy of J1429+5447 is likely a merger. J2318–3113 is another known from the literature (Neeleman et al. 2021) radio-loud quasar hosted in galaxy merger. This makes the fraction of mergers among host galaxies of radio-loud quasars $> 40\%$ at $z > 6$ only marginally higher than of radio-quiet quasars. Since our current data do not allow us to determine whether the host galaxies of the remaining three quasars are mergers, no conclusions can be made about the evolution of the merger fraction with redshift.

The [CII] and IR luminosity distributions of radio-loud quasars is comparable with that of radio-quiet quasars. If the [CII] emission and underlying continuum emission is only linked to the SFR in the host galaxy, the properties of host galaxies of radio-loud quasars are similar to the radio-quiet population covering the same range of SFRs. However, several other sources of [CII] and IR emission can be present in radio-loud quasars presented in this paper. The FIR flux can include contribution from the synchrotron emission to FIR flux and [CII] emission possibly originates from XDR or the shocks from interaction between the jet and the ISM. If this is the case, the SFRs of the host galaxies are overestimated and can be lower than in radio-quiet quasars. This would imply a negative feedback from the jet.

Acknowledgements. Based on observations carried out under project number S19DN and S20CY with the IRAM NOEMA Interferometer. IRAM is supported by INSU/CNRS (France), MPG (Germany) and IGN (Spain). S.R.R. Acknowledges financial support from the International Max Planck Research School for Astronomy and Cosmic Physics at the University of Heidelberg (IMPRS-HD).

References

Andika, I. T., Jahnke, K., Onoue, M., et al. 2020, ApJ, 903, 34
Appleton, P. N., Diaz-Santos, T., Fadda, D., et al. 2018, ApJ, 869, 61
Appleton, P. N., Guillard, P., Boulanger, F., et al. 2013, ApJ, 777, 66
Bañados, E., Carilli, C., Walter, F., et al. 2018a, ApJ, 861, L14
Bañados, E., Decarli, R., Walter, F., et al. 2015a, ApJ, 805, L8
Bañados, E., Mazzucchelli, C., Momjian, E., et al. 2021, ApJ, 909, 80
Bañados, E., Venemans, B. P., Mazzucchelli, C., et al. 2018b, Nature, 553, 473
Bañados, E., Venemans, B. P., Morganson, E., et al. 2015b, ApJ, 804, 118
Beelen, A., Cox, P., Benford, D. J., et al. 2006, ApJ, 642, 694
Belladitta, S., Moretti, A., Caccianiga, A., et al. 2020, A&A, 635, L7
Bischetti, M., Maiolino, R., Carniani, S., et al. 2019, A&A, 630, A59
Boogaard, L., Meyer, R. A., & Novak, M. 2021, Interferopy: analysing datacubes from radio-to-submm observations
Carilli, C. L. & Walter, F. 2013, ARA&A, 51, 105
Chabrier, G. 2003, Publications of the Astronomical Society of the Pacific, 115, 763
Chiaberge, M., Gilli, R., Lotz, J. M., & Norman, C. 2015, ApJ, 806, 147
Cicone, C., Maiolino, R., Gallerani, S., et al. 2015, A&A, 574, A14
Condon, J. J., Cotton, W. D., Greisen, E. W., et al. 1998, AJ, 115, 1693
Connor, T., Bañados, E., Stern, D., et al. 2021, ApJ, 911, 120
Conway, J. E. 2002, New A Rev., 46, 263
da Cunha, E., Groves, B., Walter, F., et al. 2013, ApJ, 766, 13
De Looze, I., Cormier, D., Lebouteiller, V., et al. 2014, A&A, 568, A62
Decarli, R., Walter, F., Venemans, B. P., et al. 2017, Nature, 545, 457
Decarli, R., Walter, F., Venemans, B. P., et al. 2018, ApJ, 854, 97
Di Matteo, T., Springel, V., & Hernquist, L. 2005, Nature, 433, 604
Dunne, L., Eales, S. A., & Edmunds, M. G. 2003, MNRAS, 341, 589
Eilers, A.-C., Hennawi, J. F., Decarli, R., et al. 2020, ApJ, 900, 37
Frey, S., Gurvits, L. I., Paragi, Z., & É. Gabányi, K. 2008, A&A, 484, L39
Frey, S., Paragi, Z., Gurvits, L. I., Gabányi, K. É., & Cseh, D. 2011, A&A, 531, L5
Högbom, J. A. 1974, A&AS, 15, 417
Ighina, L., Belladitta, S., Caccianiga, A., et al. 2021, arXiv e-prints, arXiv:2101.11371
Inayoshi, K., Visbal, E., & Haiman, Z. 2020, ARA&A, 58, 27
Intema, H. T., Jagannathan, P., Mooley, K. P., & Frail, D. A. 2017, A&A, 598, A78
Izumi, T., Onoue, M., Matsuoka, Y., et al. 2019, PASJ, 71, 111
Izumi, T., Onoue, M., Shirakata, H., et al. 2018, PASJ, 70, 36
Jolley, E. J. D. & Kuncic, Z. 2008, MNRAS, 386, 989
Kass, R. E. & Raftery, A. E. 1995, Journal of the American Statistical Association, 90, 773
Kellermann, K. I., Sramek, R., Schmidt, M., Shaffer, D. B., & Green, R. 1989, AJ, 98, 1195
Kennicutt, Robert C., J. 1998, ApJ, 498, 541
Liu, Y., Wang, R., Momjian, E., et al. 2021, ApJ, 908, 124
Maiolino, R., Cox, P., Caselli, P., et al. 2005, A&A, 440, L51
Maiolino, R., Gallerani, S., Neri, R., et al. 2012, MNRAS, 425, L66
Mandal, A., Mukherjee, D., Federrath, C., et al. 2021, MNRAS[arXiv:2109.13654]
McGreer, I. D., Becker, R. H., Helfand, D. J., & White, R. L. 2006, ApJ, 652, 157
Medvedev, P., Gilfanov, M., Sazonov, S., Schartel, N., & Sunyaev, R. 2021, MNRAS, 504, 576
Medvedev, P., Sazonov, S., Gilfanov, M., et al. 2020, MNRAS, 497, 1842
Meijerink, R., Spaans, M., & Israel, F. P. 2007, A&A, 461, 793
Meyer, R. A., Walter, F., Cicone, C., et al. 2022, arXiv e-prints, arXiv:2201.08143
Momjian, E., Bañados, E., Carilli, C. L., Walter, F., & Mazzucchelli, C. 2021, AJ, 161, 207
Momjian, E., Carilli, C. L., & McGreer, I. D. 2008, AJ, 136, 344
Neeleman, M., Novak, M., Venemans, B. P., et al. 2021, ApJ, 911, 141
Novak, M., Venemans, B. P., Walter, F., et al. 2020, ApJ, 904, 131
Pensabene, A., Decarli, R., Bañados, E., et al. 2021, A&A, 652, A66
Peterson, B. W., Appleton, P. N., Bitsakis, T., et al. 2018, ApJ, 855, 141
Rojas-Ruiz, S., Bañados, E., Neeleman, M., et al. 2021, ApJ, 920, 150
Shen, Y., Wu, J., Jiang, L., et al. 2019, ApJ, 873, 35
Shimwell, T. W., Tasse, C., Hardcastle, M. J., et al. 2019, A&A, 622, A1
Silk, J. 2013, ApJ, 772, 112
Smirnova-Pinchukova, I., Husemann, B., Busch, G., et al. 2019, A&A, 626, L3
Venemans, B. P., McMahon, R. G., Walter, F., et al. 2012, ApJ, 751, L25
Venemans, B. P., Walter, F., Decarli, R., et al. 2017, ApJ, 851, L8
Venemans, B. P., Walter, F., Neeleman, M., et al. 2020, ApJ, 904, 130
Venemans, B. P., Walter, F., Zschaechner, L., et al. 2016, ApJ, 816, 37
Villar Martín, M., Emonts, B., Humphrey, A., Cabrera Lavers, A., & Binette, L. 2014, MNRAS, 440, 3202
Volonteri, M., Habouzit, M., & Colpi, M. 2021, arXiv e-prints, arXiv:2110.10175
Volonteri, M., Silk, J., & Dubus, G. 2015, ApJ, 804, 148
Walter, F., Riechers, D., Cox, P., et al. 2009, Nature, 457, 699
Wang, F., Yang, J., Fan, X., et al. 2021, ApJ, 907, L1
Wang, R., Wagg, J., Carilli, C. L., et al. 2013, ApJ, 773, 44
Wang, R., Wagg, J., Carilli, C. L., et al. 2011, ApJ, 739, L34
Wang, R., Wu, X.-B., Neri, R., et al. 2016, ApJ, 830, 53
Willott, C. J., Bergeron, J., & Omont, A. 2015, ApJ, 801, 123
Willott, C. J., Bergeron, J., & Omont, A. 2017, ApJ, 850, 108
Willott, C. J., Delorme, P., Reylé, C., et al. 2010, AJ, 139, 906
Willott, C. J., Omont, A., & Bergeron, J. 2013, ApJ, 770, 13
Yang, J., Venemans, B., Wang, F., et al. 2019, ApJ, 880, 153
Yang, J., Wang, F., Fan, X., et al. 2020, ApJ, 897, L14